# Lawrence Berkeley National Laboratory
## LBL Publications

### Title
Charge Density Wave Order and Electronic Phase Transitions in a Dilute d-Band Semiconductor

### Permalink
https://escholarship.org/uc/item/9jg0z5x0


### Journal
Advanced Materials, 35(49)

### ISSN
0935-9648


### Authors
Chen, Huandong
Zhao, Boyang
Mutch, Josh
et al.


### Publication Date
2023-12-01

### DOI
10.1002/adma.202303283


### Copyright Information
This work is made available under the terms of a Creative Commons Attribution License, available at https://creativecommons.org/licenses/by/4.0/

Peer reviewed

eScholarship.org Powered by the California Digital Library
University of California

Check for updates



ADVANCED MATERIALS
www.advmat.de

# Charge Density Wave Order and Electronic Phase Transitions in a Dilute *d*-Band Semiconductor

*Huandong Chen, Boyang Zhao, Josh Mutch, Gwan Yeong Jung, Guodong Ren, Sara Shabani, Eric Seewald, Shanyuan Niu, Jiangbin Wu, Nan Wang, Mythili Surendran, Shantanu Singh, Jiang Luo, Sanae Ohtomo, Gemma Goh, Bryan C. Chakoumakos, Simon J. Teat, Brent Melot, Han Wang, Abhay N. Pasupathy, Rohan Mishra, Jiun-Haw Chu, and Jayakanth Ravichandran**

**As one of the most fundamental physical phenomena, charge density wave (CDW) order predominantly occurs in metallic systems such as quasi-1D metals, doped cuprates, and transition metal dichalcogenides, where it is well understood in terms of Fermi surface nesting and electron–phonon coupling mechanisms. On the other hand, CDW phenomena in semiconducting systems, particularly at the low carrier concentration limit, are less common and feature intricate characteristics, which often necessitate the exploration of novel mechanisms, such as electron–hole coupling or Mott physics, to explain. In this study, an approach combining electrical transport, synchrotron X-ray diffraction, and density-functional theory calculations is used to investigate CDW order and a series of hysteretic phase transitions in a dilute *d*-band semiconductor, $BaTiS_3$. These experimental and theoretical findings suggest that the observed CDW order and phase transitions in $BaTiS_3$ may be attributed to both electron–phonon coupling and non-negligible electron–electron interactions in the system. This work highlights $BaTiS_3$ as a unique platform to explore CDW physics and novel electronic phases in the dilute filling limit and opens new opportunities for developing novel electronic devices.**

## 1. Introduction

Charge density wave (CDW) is a periodic modulation of electron density, which is accompanied by periodic lattice distortions and is mostly observed in low-dimensional metals such as $NbSe_3$.[1] The key features of CDW derived from Peierls' model[2] include 1) Fermi surface nesting in electronic structure, 2) a Kohn anomaly in phonon spectra, 3) a structural transition with periodic lattice distortion, and 4) a metal-insulator transition with anomalies in resistivity. Many of these features can be experimentally probed using techniques such as transport, diffraction, and spectroscopy to confirm the presence of CDW, although not all of them need to be present in real CDW materials.[2b] In recent years, there has been growing interest to explore CDW systems that exhibit semiconducting transport behavior, such as 1*T*-$TaS_2$[3] and 1*T*-$TiSe_2$,[4] whose origin

H. Chen, B. Zhao, S. Niu, N. Wang, M. Surendran, S. Singh, B. Melot, J. Ravichandran
Mork Family Department of Chemical Engineering and Materials Science
University of Southern California
Los Angeles, CA 90089, USA
E-mail: j.ravichandran@usc.edu

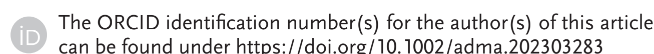
The ORCID identification number(s) for the author(s) of this article can be found under https://doi.org/10.1002/adma.202303283

© 2023 The Authors. Advanced Materials published by Wiley-VCH GmbH. This is an open access article under the terms of the Creative Commons Attribution-NonCommercial License, which permits use, distribution and reproduction in any medium, provided the original work is properly cited and is not used for commercial purposes.

**DOI: 10.1002/adma.202303283**

J. Mutch, S. Ohtomo, J.-H. Chu
Department of Physics
University of Washington
Seattle, WA 98195, USA

G. Y. Jung, R. Mishra
Department of Mechanical Engineering and Materials Science
Washington University in St. Louis
St. Louis, MO 63130, USA

G. Ren, R. Mishra
Institute of Materials Science and Engineering
Washington University in St. Louis
St. Louis, MO 63130, USA

S. Shabani, E. Seewald, A. N. Pasupathy
Department of Physics
Columbia University
New York, NY 10027, USA

 © 2023 The Authors. Advanced Materials published by Wiley-VCH GmbH

15214095, 2023, 49, Downloaded from https://onlinelibrary.wiley.com/doi/10.1002/adma.202303283, Wiley Online Library on [05/09/2024]. See the Terms and Conditions (https://onlinelibrary.wiley.com/terms-and-conditions) on Wiley Online Library for rules of use; OA articles are governed by the applicable Creative Commons License

presumably go beyond *q*-dependent electron–phonon coupling mechanism. These materials exhibit a variety of intriguing phenomena such as electron–hole coupling,[4b] resistive switching,[3b,5] toroidal dipolar structures,[6] and wide hysteretic transitions,[7] which not only lead to vigorous debates over the mechanism of these CDW transitions,[7,8] but also hold promise for new applications of CDW. Hence, exploring such novel materials that exhibit a confluence of CDW ordering and semiconducting behavior can be both scientifically and practically interesting.

Here, we report the discovery of CDW order and phase transitions in a non-degenerate semiconductor, $BaTiS_3$, which broadens the realm of CDW physics, particularly in semiconducting materials. We observe two hysteretic resistive phase transitions that correspond to the emergence and suppression of the CDW state using transport measurements. Combining single-crystal X-ray diffraction (XRD), we provide direct experimental evidence of CDW order in the system and track its evolution in both electronic and lattice degrees of freedom. Our findings suggest that a combination of electron–phonon coupling, and non-negligible electron–electron interactions may be responsible for the observed phase transitions in $BaTiS_3$. Our study establishes semiconducting $BaTiS_3$ as a new model system for investigating rich electronic phases and phase transitions in dilute filling and offers new opportunities in electronic device applications of CDW phase change materials.

## 2. Results

### 2.1. Transport Signatures of Phase Transitions in $BaTiS_3$

Quasi-1D chalcogenide, $BaTiS_3$, is a small bandgap semiconductor ($E_g \sim 0.3$ eV) with a hexagonal crystal structure composed of 1D chains of $TiS_6$ octahedra, stacked between Ba chains (**Figure 1**a). Recently, a giant optical anisotropy[9] and abnormal glass-like thermal transport properties[10] were reported in this material, which imposed questions over its electronic properties. However, as a $d^0$ semiconductor with a nominally empty conduction band, no phase transitions have been theoretically expected or experimentally observed in $BaTiS_3$ to date, although its $d^1$ counterpart, $BaVS_3$, is an archetypical CDW system.[11]

We performed electrical transport measurements on bulk single crystals of $BaTiS_3$ along the chain axis (*c*-axis) (Figure 1b). Here, we identify two different phase transitions from their non-monotonic and hysteretic transport behavior. Upon cooling, the electrical resistivity increases, and the system undergoes a phase transition at 240 K (Transition II) featuring a resistivity jump. On further cooling, it continues to increase to 150 K, after which the material undergoes another transition that we call Transition I with a sharp drop in resistivity. Transition II (240–260 K) hints at the emergence of a CDW state from a high-temperature semiconducting phase; while at Transition I (150–190 K), the CDW order is suppressed and the system switches to a more conductive state. Similar hysteretic transport behavior has been observed and well understood in many other CDW systems such as $(NbSe4)_{10}I_3$[12] and 1*T*-$TaS_2$,[13] which is primarily attributed to the interaction between CDW condensates and defects.

To further understand these observations, we performed Hall measurements to study the evolution of carrier concentration and mobility across both phase transitions (Figure 1c,d). At room temperature, the electron concentration is $\sim 1.1 \times 10^{18}$ cm$^{-3}$, and it reduces to less than $10^{15}$ cm$^{-3}$ at 100 K. These observations confirm the non-degenerate nature of $BaTiS_3$, which possesses one of the lowest carrier densities among reported CDW compounds. The overall trend of carrier concentration $n$ is dominated by the semiconducting nature of $BaTiS_3$, where it decreases monotonically as temperature is lowered and we did not observe any change in carrier type across the transitions. We further obtained thermal activation energy $E_a$ for each phase from Arrhenius analysis ( $E_a = -\delta(\ln(n))/\delta(1/k_B T)$), as illustrated in Figure S5 (Supporting Information). The extracted carrier transport activation barrier increases from 125 meV to 219 meV at Transition II, and it reduces to 117 meV across Transition I.

The Hall mobility evolution in $BaTiS_3$ (Figure 1d) follows an overall increasing trend as temperature decreases, which, however, undergoes a notable drop and then a substantial increase in mobility values across the two phase transitions, respectively. Moreover, we found that the modulation of electrical resistances during both transitions (Figure 1b) is predominantly due to the variations in Hall mobility, rather than changes in carrier concentration across the transitions. This is distinct from many other resistive switching systems that undergo a transition from a metallic phase to an insulating phase, such as $VO_2$[14] and 1*T*-$TaS_2$,[13] where the gap opening from a metal reduces the free carrier concentrations significantly, and hence, such carrier concentration modulation mechanism dominates. All these transport observations in $BaTiS_3$ are consistent with two phase transitions that lead to a sequence of electronic phases, starting from a high-temperature semiconducting phase that transitions to a reduced-mobility CDW phase at intermediate temperatures, and finally to a high-mobility phase at low temperatures.

J. Wu, H. Wang, J. Ravichandran
Ming Hsieh Department of Electrical and Computer Engineering
University of Southern California
Los Angeles, CA 90089, USA
M. Surendran, J. Ravichandran
Core Center for Excellence in Nano Imaging
University of Southern California
Los Angeles, CA 90089, USA
J. Luo
Department of Chemistry
Washington University in St. Louis
St. Louis, MO 63130, USA
G. Goh, B. Melot
Department of Chemistry
University of Southern California
Los Angeles, CA 90089, USA
B. C. Chakoumakos
Neutron Scattering Division
Oak Ridge National Laboratory
Oak Ridge, TN 37831, USA
S. J. Teat
Advanced Light Source
Lawrence Berkeley National Laboratory
Berkeley, CA 94720, USA


© 2023 The Authors. Advanced Materials published by Wiley-VCH GmbH

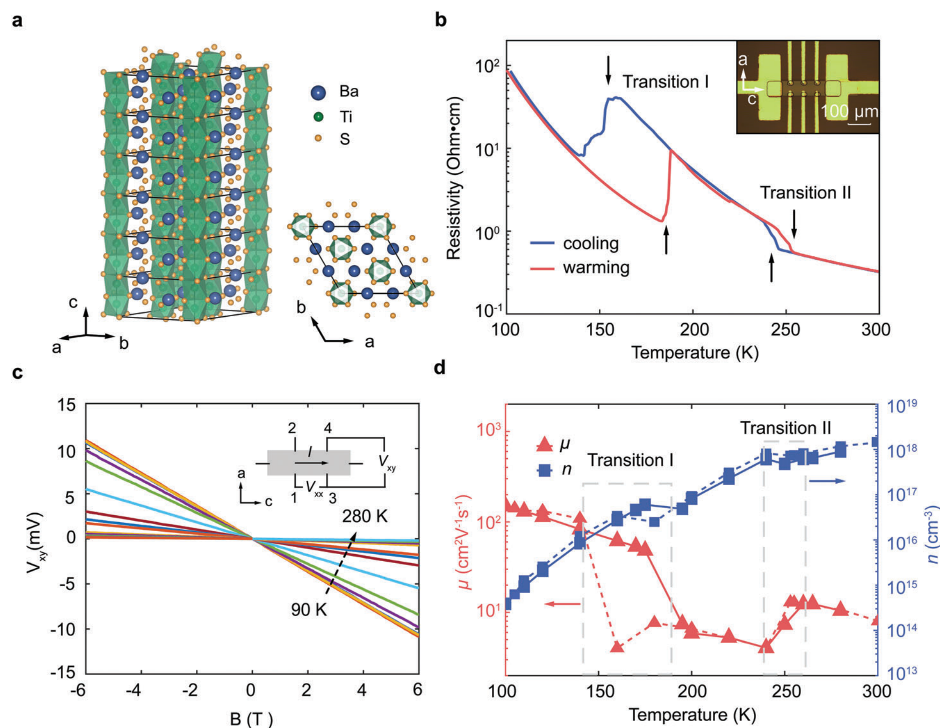


**Figure 1.** Signature of phase transitions from electrical transport measurements. a) Room temperature $P6_3cm$ structure of $BaTiS_3$, showing hexagonal symmetry. b) Illustration of representative temperature dependent electrical resistivity of $BaTiS_3$ crystal along the *c*-axis. Abrupt and hysteric jumps in resistance are shown near 150–190 K (Transition I), and 240–260 K (Transition II). Inset shows an optical microscopic image of the $BaTiS_3$ device used for Hall measurements. c) Plot of Hall voltage $V_{xy}$ with the magnetic field ranging from −6 to 6 T at different temperatures. d) Temperature dependence of the mobility, $\mu$, and carrier concentration, $n$, of the dominant carrier, extracted from Hall measurements. The solid line illustrates the data taken from a warming cycle, while the dashed line represents measurement during the cooling cycle.

### 2.2. Structural Characterization

We carried out synchrotron XRD at three representative temperatures to track the structural changes across the phase transitions and to accurately determine the structure for each phase. **Figure** 2 a-c show the precession maps of $BaTiS_3$ crystal projected onto the $hk2$ reciprocal plane at 298 K, 220 K, and 130 K respectively, and Figure 2d illustrates a zoomed-in intensity cut along the direction as indicated in the precession images. The corresponding crystal structures were solved by single crystal refinement and the detailed crystallography information are listed in the supplementary tables. At room temperature, a hexagonal array of reflection spots is observed in the precession image, which is consistent with a $P6_3cm$ space group ($a = b = 11.7$ Å, $c = 5.83$ Å). Upon cooling to 220 K, additional superlattice reflections that are two orders of magnitude lower than primary reflections appear at $h + 1/2\ k + 1/2\ 2$, indicating a change in the periodicity of the lattice ($a = b = 23.3$ Å, $c = 5.84$ Å) associated with Transition II from $P6_3cm$ to $P3c1$. Complementary to the resistivity anomalies observed from transport measurements, the weak superlattice reflections in diffraction patterns provide one of the most convincing experimental evidence of CDW formation in $BaTiS_3$ below Transition II. These satellite peaks stem from periodic lattice distortions that are directly associated with charge modulation.[15] Interestingly, the unit cell doubling in $BaTiS_3$ takes place in the $a$–$b$ plane, rather than along the chain axis (*c*-axis), which is usually the case in many other classic quasi-1D CDW systems such as $NbSe_3$[16] and $BaVS_3$.[17] Moreover, the space group symmetries of the two phases ($P6_3cm$ and $P3c1$) show a group/subgroup relationship. Hence, Transition II can be classified as a displacive transition, according to Buerger's classification of phase transitions,[18] which tends to show second-order or weak first-order thermodynamic characteristics, consistent with the small thermal hysteresis observed from transport measurements.

On further lowering the temperature to 130 K, the superlattice peaks disappeared, and a new set of reflections associated with a smaller $\frac{2}{\sqrt{3}} \times \frac{2}{\sqrt{3}}$ unit cell emerged ($a = b = 13.4$ Å, $c = 5.82$ Å), which indicates a direct suppression of the CDW via the structural transition ($P3c1$ to $P2_1$). The low-temperature space group $P2_1$ is not a subgroup of $P3c1$, and we have observed the large thermal hysteresis (~40 K) from transport measurements, both of which lead us to conclude that the Transition I is a reconstructive transition,[18] where first-order thermodynamic characteristics, such as thermal hysteresis, coexistence of phases at equilibrium, and metastability, are often expected. The observed intermediate steps of Transition I from transport measurements (Figure 1b; Figure S4a, Supporting Information) are also attributed to the percolative nature of the reconstructive structural transition. An evolution of unit cell sizes in $BaTiS_3$ is summarized in **Figure 3**c.

 © 2023 The Authors. Advanced Materials published by Wiley-VCH GmbH

15214095, 2023, 49, Downloaded from https://onlinelibrary.wiley.com/doi/10.1002/adma.202303283, Wiley Online Library on [05/09/2024]. See the Terms and Conditions (https://onlinelibrary.wiley.com/terms-and-conditions) on Wiley Online Library for rules of use; OA articles are governed by the applicable Creative Commons License

15214095, 2023, 49, Downloaded from https://onlinelibrary.wiley.com/doi/10.1002/adma.202303283, Wiley Online Library on [05/09/2024]. See the Terms and Conditions (https://onlinelibrary.wiley.com/terms-and-conditions) on Wiley Online Library for rules of use; OA articles are governed by the applicable Creative Commons License

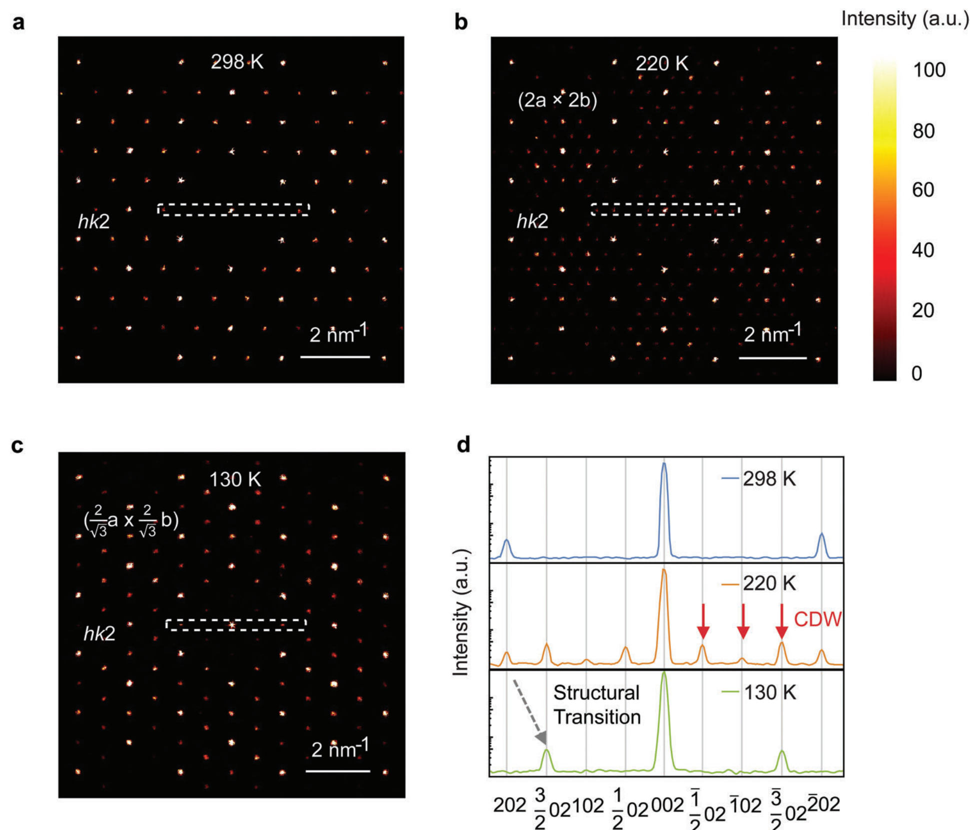


**Figure 2.** CDW order evolution revealed by single crystal X-ray diffraction of $BaTiS_3$. a–c) Reciprocal precession images of $BaTiS_3$ crystal along *hk*2 projection at 298 K, 220 K, and 130 K, respectively. d) X-ray intensity cut along the direction as indicated in the precession maps.

### 2.3. Mechanism of Phase Transitions in $BaTiS_3$

To further gain insights into the change of electronic structures in $BaTiS_3$ across these transitions, we calculated the electronic band structure of these three phases, based on refined crystal structures obtained from XRD, using density-functional theory (DFT) (Figure 3a). As the temperature is lowered, the bandgap of the system increases from 0.26 eV to 0.3 eV at Transition II and then drops to 0.15 eV across Transition I (Figure 3b), which qualitatively agrees with the evolution of the thermal activation barrier from Arrhenius analysis of transport data (Figure S5, Supporting Information).

In a gapped semiconductor such as $BaTiS_3$, as revealed by both optical spectroscopy measurements and calculated electronic band structures, the Fermi level falls in the bandgap and therefore there is no Fermi surface. Hence, the surface nesting mechanism, which is the dominant explanation for CDW in quasi-1D metals,[16] can be ruled out. One interesting observation in $BaTiS_3$ is its two-dimensional charge ordering in the *a*-*b* plane (Figure 2), rather than along the 1D chain-axis. This mismatch in dimensionality further complicates the understanding of CDW order in this material. To investigate the role of interchain coupling in stabilizing the CDW phase in $BaTiS_3$, we performed in-plane conductivity anisotropy measurements (Figure S6, Supporting Information) using Montgomery analysis.[19] The measured anisotropy in resistivity ($\rho_a/\rho_c$) was approximately 4, which is relatively small compared to other model quasi-1D CDW systems like $NbSe_3$ ($\rho_a/\rho_c \sim$ 15–20)[20] and $(TaSe_4)_2I$ ($\rho_a/\rho_c > 200$).[21]

In many real CDW materials, the CDW order is usually attributed to strong electron–phonon coupling,[22] while clean semiconductor systems typically lack such coupling. To estimate the strength of electron–phonon interaction in $BaTiS_3$, we calculated its Fröhlich coupling constant $\alpha = \frac{e^2}{4\pi\hbar}\left(\frac{1}{\varepsilon_\infty} - \frac{1}{\varepsilon_s}\right)\sqrt{\frac{m_b}{2\hbar\omega_0}}$ for each phase[23] (Table S1, Supporting Information), where the effective mass $m_b$, static and high-frequency dielectric constant $\varepsilon_s$ and $\varepsilon_\infty$, and the effective polar optical phonon angular frequency $\omega_0$ were obtained from DFT. The calculated $\alpha$ values of $BaTiS_3$ are 1.36, 1.79 and 1.64 for the $P6_3cm$, $P3c1$, and $P2_1$ phases, respectively, indicating intermediate to relatively strong electron–phonon coupling systems. For comparison, the reported $\alpha$ values for semiconductors such as GaAs, and InP are typically well below 1.[24] Moreover, the evolution of carrier mobility observed in $BaTiS_3$ (Figure 1d) can also be qualitatively understood in terms of electron–phonon coupling, considering the polar optical phonon (POP) scattering as the major scattering mechanism in that temperature range. The overall increasing trend of Hall mobility ($\mu = e\tau/m_b$) is consistent with a scheme of reduced phonon scattering rate ($1/\tau_{POP}$) at lower temperature, while a smaller mobility value is expected for the $P3c1$ phase, considering its larger $\alpha$ value (stronger electron–phonon interactions,


© 2023 The Authors. Advanced Materials published by Wiley-VCH GmbH

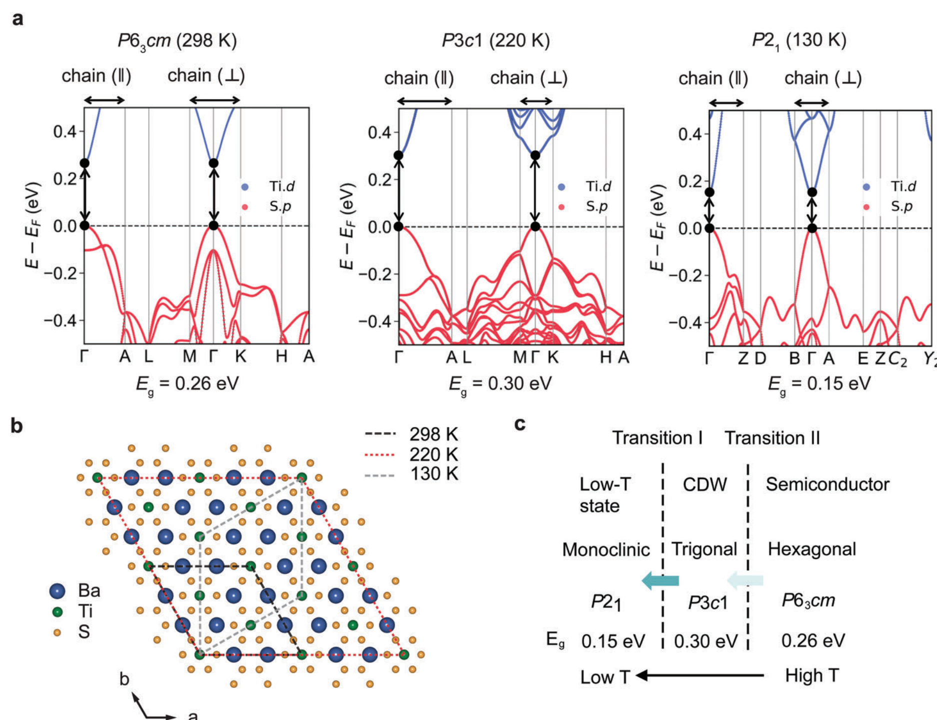


**Figure 3.** a) DFT-calculated electronic band structures of different phases of $BaTiS_3$. The contribution of Ti *d*-states and S *p*-states to the band structure are highlighted with blue and red colors, respectively. The band gap ($E_g$) calculated at the PBE level is provided underneath the plots. The vertical arrows indicate the changing band gap at the Γ point. The horizontal arrows show the symmetry direction along chain-parallel- ('chain(||)') and chain-perpendicular-plane ('chain(⊥)') from the zone-center (Γ point) in the first Brillouin zone. b) Illustration of unit cell evolution of $BaTiS_3$ at different temperatures. c) Summary of electronic phases and phase transitions in $BaTiS_3$.

and hence, smaller scattering time), and a larger effective mass $m_b$, compared with the other two phases.

Furthermore, as a non-degenerate semiconductor with a dilute concentration of electrons, the role of electron–electron interaction in $BaTiS_3$ could be non-trivial, unlike most metallic or semi-metallic CDW systems. One way to evaluate the electron correlation effects in a material is by calculating the dimensionless parameter $r_s = \sqrt[3]{\frac{1}{\frac{4}{3}\pi n}}/(\frac{4\pi\varepsilon\hbar^2}{m_b e^2})$, defined by the ratio of Wigner-sphere radius (dominated by electron–electron interaction) to Bohr radius for a 3D electronic system.[25] Using the experimentally measured carrier concentration $n$, calculated band effective mass for electrons $m_b$ and static dielectric constant ε from DFT, we obtained $r_s$ value of $BaTiS_3$ close to 4.4 at 200 K ($n = 8.2 \times 10^{16}$ $cm^{-3}$), and it further reaches 18.5 at 90 K ($n = 1.7 \times 10^{14}$ $cm^{-3}$) (Table S1, Supporting Information). Although the calculated $r_s$ values are still away from strongly correlated region ($r_s$ values ~ 100)[25] within the temperature range of transitions, one cannot fully rule out the role of the correlation effects like in other metallic CDW systems. For comparison, the calculated $r_s$ parameters of many metallic CDW systems tend to be very small (close to zero, Table S2, Supporting Information) primarily due to high carrier concentrations and large dielectric constants, which is also in line with the negligible electron–electron interactions in those systems. Therefore, the origin of CDW order and phase transitions in semiconducting $BaTiS_3$ can be potentially attributed to the combined effects of electron–lattice and electron–electron interactions.

## 3. Conclusion

In summary, we have investigated the CDW order and phase transitions in a dilute *d*-band semiconductor, $BaTiS_3$, by combining transport, XRD measurements, and DFT calculations. Several groups in the past have also studied the physical properties of $BaTiS_3$ compound at cryogenic temperatures,[9,10,26] but no phase transition was reported before. This is mainly because careful and advanced characterizations are needed to probe the subtle signatures of intrinsic phase transitions while by that time no one was expecting their existence in such a semiconducting system. Moreover, we have found that $BaTiS_3$ is very sensitive to external stimuli such as strain and the phase transitions can be easily shifted or even smeared thereby, as illustrated in Figure S11 (Supporting Information). Hence, good control over $BaTiS_3$ single crystal synthesis, the employment of high-flux XRD characterization, an improvement on device fabrication, and strain-free transport measurements have allowed us to observe those phase transitions reliably in this work.

The phase transitions in $BaTiS_3$ show several peculiar features: i) the CDW phase emerges from a semiconducting phase with a low carrier density, ii) the structural transition (Transition II) features an abrupt switching toward a more conductive state upon cooling, iii) Transition II has a large thermal hysteresis window of over 40 K, iv) the changes of electrical resistance across both transitions are mainly due to the modulation of Hall mobility, rather than carrier concentrations, and (v) the CDW ordering is two dimensional and the electronic anisotropy of $BaTiS_3$ is relatively


© 2023 The Authors. Advanced Materials published by Wiley-VCH GmbH

15214095, 2023, 49, Downloaded from https://onlinelibrary.wiley.com/doi/10.1002/adma.202303283, Wiley Online Library on [05/09/2024]. See the Terms and Conditions (https://onlinelibrary.wiley.com/terms-and-conditions) on Wiley Online Library for rules of use; OA articles are governed by the applicable Creative Commons License

15214095, 2023, 49, Downloaded from https://onlinelibrary.wiley.com/doi/10.1002/adma.202303283, Wiley Online Library on [05/09/2024]. See the Terms and Conditions (https://onlinelibrary.wiley.com/terms-and-conditions) on Wiley Online Library for rules of use; OA articles are governed by the applicable Creative Commons License

small, although structurally and optically being very anisotropic. Our analysis suggests that CDW order and phase transitions in semiconducting $BaTiS_3$ may be contributed by both electron-lattice interactions and non-negligible elector–electron interactions. Further experimental and theoretical studies are necessary to probe the evolution of electronic structure and phonon dispersion across the transitions, to pin down the origin or driving force of these transitions. Responses of the phase transitions in $BaTiS_3$ to external fields such as pressure, strain, and doping, and the possible emergence of electronic phases such as superconductivity are also of interest.

In addition, while CDW phenomena have been extensively studied in various materials systems, practical electronic device applications based on CDW are still limited due to the absence of pronounced hysteretic resistive transitions in most CDW systems. One notable exception is the quasi-2D Mott insulator 1*T*-$TaS_2$, where the hysteretic CDW phase transitions have been utilized to develop novel electronics such as phase change oscillators[27] and memory devices.[5,28] In $BaTiS_3$, we have demonstrated two hysteretic resistive phase transitions, one of which is close to first-order and the other presumably second-order, making it an ideal candidate for achieving both non-volatile and volatile type resistive switching in the system. We anticipate that these phase transitions in $BaTiS_3$ will offer new opportunities for achieving neuromorphic functionalities, similar to what has been achieved with 1*T*-$TaS_2$. Further research in this direction is necessary to explore the full potential of CDW-based electronic devices using $BaTiS_3$.

## 4. Experimental Section

*Crystal Growth and Room Temperature Characterization*: Single crystals of $BaTiS_3$ were grown by the chemical vapor transport method as reported elsewhere.[9] Figure S1 (Supporting Information) illustrates different morphologies of the obtained crystals with *a*- and *c*-axis in-plane. Single-crystal diffraction performed at room temperature showed no substantial differences structurally between them (Table S4, Supporting Information). Needle-like crystals with well-defined *c*-axis were usually picked for transport measurements. For in-plane transport anisotropy measurements, as well as all temperature-dependent optical and single-crystal XRD characterization in this manuscript, $BaTiS_3$ platelet samples were used.

Scanning tunneling microscopy and scanning tunneling spectroscopy measurements were performed on a freshly cleaved surface of a needle sample at room temperature (Figure S2, Supporting Information). The surface morphology scan clearly resolved the crystal surface with RMS roughness less than 0.5 nm. Figure S2b (Supporting Information) illustrates the $dI/dV$ spectra of $BaTiS_3$. It should be noted that the extraction of the semiconducting gap from such experimental tunneling spectra is, in general, difficult due to thermal broadening at room temperature and the presence of defects that contribute in-gap states to the $dI/dV$ spectra. For reference, both the reported optical absorption spectra[9] and DFT calculations gave ~0.3 eV gap size.

*Device Fabrication*: As-grown $BaTiS_3$ crystals (10–20 µm thick, ~300 µm long) were embedded in a polymeric media to planarize the top surface[29] such that regular lithography and metallization methods could be readily applied, as illustrated in Figure S3a (Supporting Information). Low-stress polyimide (PI) with a coefficient of thermal expansion (CTE) ~$3 \times 10^{-6}$ $K^{-1}$ was chosen to minimize the effect of thermal contraction on $BaTiS_3$ transport behaviors at low temperatures. Vertical interconnect access holes of the same PI dielectric layer were fabricated using photolithography and RIE etch ($O_2/CF_4$ = 45/5 sccm, 100 W, 100 mTorr, 2 min), in order to precisely define the contacting area and to encapsulate the $BaTiS_3$ channels. Ohmic contacts to $BaTiS_3$ crystals were fabricated by regular e-beam evaporation of Ti/Au (3/300 nm) and lift-off. An $SF_6$/Ar RIE treatment step (10/40 sccm, 100 W, 100 mTorr, 1 min) was applied right before the metal deposition to remove surface oxides and further reduce the contact resistance. Optical images of $BaTiS_3$ devices are shown in Figure S3b (Supporting Information). Transport measurements shown in Figure S4b (Supporting Information) were carried out on long needle-like $BaTiS_3$ crystals (a few mm long) contacted by pre-sputtered Au film and hand bonding using Ag epoxy and Au wires, which is considered stress-free. The polyimide embedding method was developed for the purpose of performing multi-terminal transport measurements on small, thick bulk crystals such as $BaTiS_3$. The technical details of this method were presented elsewhere.[29] The following criteria were adopted to determine whether the crystal was in nearly strain-free status: 1) the transport behavior was consistent with the conventional hand bonding contacting method using silver epoxy and Au wires, and 2) the transport behavior was reproducible between different heating/cooling cycles, as presented in Figure S4b,c (Supporting Information).

*Electrical Transport Measurements and Analysis*: Standard low-frequency ($f$ = 17 Hz) AC lock-in techniques (Stanford Research SR830) were used to measure sample resistance in four-probe geometry, with an excitation current of about 100 nA. Regular transport measurements were carried out in a JANIS 10 K closed-cycle cryostat from 100 K to 300 K. Qualitatively reproducible transport behavior showing two characteristic phase transitions were obtained from several devices, with different cooling cycles/cooling rates, and different fabrication methods as shown in Figure S4 (Supporting Information).

In-plane conductivity anisotropy was assessed by the Montgomery method[19] (Figure S7a,b, Supporting Information). The analysis was carried out by using a van der Pauw geometry to calculate the conductivity anisotropy $\rho_a/\rho_c$ using $(\frac{l}{w})^2 \times B^2_{\alpha,k}$, where $l$ and $w$ are sample dimensions and $B_{\alpha,k}$ is the conformal mapping function related to the ratio of van der Pauw resistance along different directions ($R_{aa}/R_{cc}$). The extracted anisotropy value is close to 4 at room temperature.

Hall measurements were performed in a PPMS (Quantum Design) equipped with a 14 T magnet. AC current was generated by a lock-in amplifier and passed through the device, $V_{xx}$, $V_{xy}$ as well as the current $I_{AC}$ were recorded simultaneously. Carrier concentration $n$ and mobility $\mu$ were extracted assuming a single carrier model. Figure S8 (Supporting Information) shows supplemental data from magneto-transport measurement. Unlike many other metallic CDW systems such as 2*H*-$NbSe_2$[30] and 1*T*-$TiSe_2$,[15a] no carrier-type switching behavior was observed across either of the two phase transitions, indicated by the plot of Hall voltage $V_{xy}$ versus $B$ throughout the whole temperature range.

*Single Crystal X-Ray Diffraction*: Single crystal X-ray diffraction at 130 K, 220 K, and 298 K were carried out on beamline 12.2.1 at the Advanced Light Source, Lawrence Berkeley National Laboratory. Crystals were mounted on MiTeGen Kapton loops (Dual Thickness MicroMounts$^{TM}$) and placed in a nitrogen cold stream on the goniometer head of a Bruker D8 diffractometer, equipped with a PHOTONII CPAD detector operating in shutter-less mode. Diffraction data were collected using monochromatic synchrotron radiation with a wavelength of 0.72880 Å using a silicon (111) monochromator. A combination of $f$ and $\omega$ scans with scan speeds of 1 s per 2° for the $f$ scans and 1 s per 0.15° for the $\omega$ scans at $2\theta = 0$ and $-20°$, respectively. The precession map was generated by Bruker APEX 3 with a resolution 1.5 Å and thickness 0.1 with the refined unit cell. Note that the refined space group was different from previously reported $P6_3/mmc$ or $P6_3mc$.[9] It is mainly attributed to the improved brightness and resolution using synchrotron radiation that allow the observation of weak reflections. Detailed crystallography data and refinement results at different temperatures are listed in Tables S3–S10 (Supporting Information).

*DFT Calculations*: The band structure of $BaTiS_3$ in the three different phases was computed using DFT. The initial structures were taken from the refined crystal structures from XRD at different temperatures, which were assigned to have a space group of $P6_3cm$ (298 K), $P3c1$ (220 K), and $P2_1$ (130 K), respectively. The structures were fully optimized by DFT. These calculations were done using the Vienna Ab initio Simulation


© 2023 The Authors. Advanced Materials published by Wiley-VCH GmbH

15214095, 2023, 49, Downloaded from https://onlinelibrary.wiley.com/doi/10.1002/adma.202303283, Wiley Online Library on [05/09/2024]. See the Terms and Conditions (https://onlinelibrary.wiley.com/terms-and-conditions) on Wiley Online Library for rules of use; OA articles are governed by the applicable Creative Commons License

Package[31] with projector-augmented wave potentials.[32] The exchange-correlation energy was treated with the generalized gradient approximation (GGA) using the Perdew–Burke–Ernzerhof (PBE) functional.[33] A cutoff energy of 650 eV was used for the expansion of the plane waves. The convergence criteria were set to $10^{-8}$ eV for total energy and $10^{-4}$ eV Å$^{-1}$ for atomic forces, respectively. The Brillouin zone was sampled using a Γ-centered Monkhorst–Pack *k*-points mesh,[34] with a maximum spacing of 0.05 Å$^{-1}$ for structural relaxations and 0.02 Å$^{-1}$ for static calculations, respectively. To address the concern related to any potential artifacts during the calculation using PBE functional, the current band structure (Figure 3a) with that calculated using the meta-generalized gradient approximation (meta-GGA) SCAN functional and with a Hubbard *U* correction (2.0 to 4.0 eV for Ti) to PBE was compared, as shown in Figures S9,S10 (Supporting Information). All three functionals (PBE, SCAN, and PBE + *U*) gave similar shifts in the conduction and valence bands for the three phases, without any band inversion. Hence, the current trend in the change in band gap for the three phases is believed valid.

For the calculation of the $r_s$ parameter, density functional perturbation theory calculations[35] were performed to obtain the static dielectric constant (ε) with the same energy cutoff and *k*-point sampling as the DFT calculations. The input parameters for $\alpha$ and $r_s$, such as the effective mass ($m_b^*$), experimental carrier concentration (*n*), static and high-frequency dielectric constant ($\varepsilon_s$ and $\varepsilon_\infty$), and effective polar optical phonon angular frequency $\omega_0$ are provided in Table S1 (Supporting Information).

## Supporting Information

Supporting Information is available from the Wiley Online Library or from the author.

## Acknowledgements

This work was supported by the Army Research Office (ARO) under award numbers W911NF-21-1-0327 (ARO MURI) and W911NF-19-1-0137 and the National Science Foundation (NSF) of the United States under award numbers DMR-2122070 and 2122071. J.M., S.O., and J.-H.C. acknowledge the support of the David and Lucile Packard Foundation and the State of Washington-funded Clean Energy Institute. This research used resources from the Advanced Light Source, which is a Department of Energy (DOE) Office of Science User Facility under contract No. DE-AC02-05CH11231. This work used computational resources through allocation DMR-160007 from the Advanced Cyberinfrastructure Coordination Ecosystem: Service & Support program, which is supported by NSF. A portion of this research used resources at the Spallation Neutron Source, a DOE Office of Science User Facility operated by the Oak Ridge National Laboratory.

## Conflict of Interest

The authors declare no conflict of interest.

## Data Availability Statement

The data that support the findings of this study are available from the corresponding author upon reasonable request.

## Keywords

charge density wave, phase transitions, quasi-1D chalcogenide, semiconductors

Received: April 8, 2023
Revised: July 31, 2023
Published online: October 27, 2023

[1] a) G. Grüner, *Rev. Mod. Phys.* **1988**, *60*, 1129; b) R. E. Peierls, *Quantum theory of solids*, Clarendon University Press, Oxford **1955**; c) R. E. Thorne, *Phys. Today* **1996**, *49*, 42.
[2] a) X. Zhu, Y. Cao, J. Zhang, E. Plummer, J. Guo, *Proc. Natl. Acad. Sci. U. S. A.* **2015**, *112*, 2367; b) X. Zhu, J. Guo, J. Zhang, E. Plummer, *Adv. Phys.: X* **2017**, *2*, 622.
[3] a) B. Sipos, A. F. Kusmartseva, A. Akrap, H. Berger, L. Forró, E. Tutiš, *Nat. Mater.* **2008**, *7*, 960; b) L. Stojchevska, I. Vaskivskyi, T. Mertelj, P. Kusar, D. Svetin, S. Brazovskii, D. Mihailovic, *Science* **2014**, *344*, 177.
[4] a) H. Cercellier, C. Monney, F. Clerc, C. Battaglia, L. Despont, M. Garnier, H. Beck, P. Aebi, L. Patthey, H. Berger, *Phys. Rev. Lett.* **2007**, *99*, 146403; b) T. Kidd, T. Miller, M. Chou, T.-C. Chiang, *Phys. Rev. Lett.* **2002**, *88*, 226402.
[5] M. Yoshida, R. Suzuki, Y. Zhang, M. Nakano, Y. Iwasa, *Sci. Adv.* **2015**, *1*, e1500606.
[6] a) A. Nakano, T. Hasegawa, S. Tamura, N. Katayama, S. Tsutsui, H. Sawa, *Phys. Rev. B* **2018**, *98*, 045139; b) S. Kitou, A. Nakano, S. Kobayashi, K. Sugawara, N. Katayama, N. Maejima, A. Machida, T. Watanuki, K. Ichimura, S. Tanda, *Phys. Rev. B* **2019**, *99*, 104109.
[7] B. Lv, A. Zong, D. Wu, A. Rozhkov, B. V. Fine, S.-D. Chen, M. Hashimoto, D.-H. Lu, M. Li, Y.-B. Huang, *Phys. Rev. Lett.* **2022**, *128*, 036401.
[8] K. Rossnagel, L. Kipp, M. Skibowski, *Phys. Rev. B* **2002**, *65*, 235101.
[9] S. Niu, G. Joe, H. Zhao, Y. Zhou, T. Orvis, H. Huyan, J. Salman, K. Mahalingam, B. Urwin, J. Wu, *Nat. Photonics* **2018**, *12*, 392.
[10] B. Sun, S. Niu, R. P. Hermann, J. Moon, N. Shulumba, K. Page, B. Zhao, A. S. Thind, K. Mahalingam, J. Milam-Guerrero, R. Haiges, M. Mecklenburg, B. C. Melot, Y.-D. Jho, B. M. Howe, R. Mishra, A. Alatas, B. Winn, M. E. Manley, J. Ravichandran, A. J. Minnich, *Nat. Commun.* **2020**, *11*, 6039.
[11] S. Fagot, P. Foury-Leylekian, S. Ravy, J. P. Pouget, H. Berger, *Phys. Rev. Lett.* **2003**, *90*, 196401.
[12] A. Smontara, K. Biljakovic, J. Mazuer, P. Monceau, F. Levy, *J. Phys.: Condens. Matter* **1992**, *4*, 3273.
[13] R. Inada, Y. Ōnuki, S. Tanuma, *Physica B+C* **1980**, *99*, 188.
[14] W. Rosevear, W. Paul, *Phys. Rev. B* **1973**, *7*, 2109.
[15] a) F. J. Di Salvo, D. Moncton, J. Waszczak, *Phys. Rev. B* **1976**, *14*, 4321; b) K. Tsutsumi, T. Takagaki, M. Yamamoto, Y. Shiozaki, M. Ido, T. Sambongi, K. Yamaya, Y. Abe, *Phys. Rev. Lett.* **1977**, *39*, 1675; c) D. Moncton, J. Axe, F. DiSalvo, *Phys. Rev. Lett.* **1975**, *34*, 734.
[16] J. Hodeau, M. Marezio, C. Roucau, R. Ayroles, A. Meerschaut, J. Rouxel, P. Monceau, *J. Phys. C: Solid State Phys.* **1978**, *11*, 4117.
[17] T. Inami, K. Ohwada, H. Kimura, M. Watanabe, Y. Noda, H. Nakamura, T. Yamasaki, M. Shiga, N. Ikeda, Y. Murakami, *Phys. Rev. B* **2002**, *66*, 073108.
[18] M. J. Buerger, *Phase transformations in solids*, John Wiley, New York **1951**, 183.
[19] a) H. Montgomery, *J. Appl. Phys.* **1971**, *42*, 2971; b) K. A. Borup, K. F. Fischer, D. R. Brown, G. J. Snyder, B. B. Iversen, *Phys. Rev. B* **2015**, *92*, 045210.
[20] N. P. Ong, J. Brill, *Phys. Rev. B* **1978**, *18*, 5265.
[21] A. Smontara, I. Tkalčec, A. Bilušić, M. Budimir, H. Berger, *Phys. B* **2002**, *316*, 279.
[22] M. Johannes, I. Mazin, *Phys. Rev. B* **2008**, *77*, 165135.
[23] a) J. T. Devreese, in *Encyclopedia of Applied Physics*, VCH, Weinheim **1996**; b) A. S. Alexandrov, J. T. Devreese, *Advances in polaron physics*, Vol. *159*, Springer Berlin, Heidelberg **2010**.
[24] G. Iadonisi, La Rivista del Nuovo Cimento, **1984**, *7*, 1.
[25] D. M. Ceperley, B. J. Alder, *Phys. Rev. Lett.* **1980**, *45*, 566.
[26] H. Imai, H. Wada, M. Shiga, *J. Phys. Soc. Jpn.* **1996**, *65*, 3460.


© 2023 The Authors. Advanced Materials published by Wiley-VCH GmbH

[27] a) G. Liu, B. Debnath, T. R. Pope, T. T. Salguero, R. K. Lake, A. A. Balandin, *Nat. Nanotechnol.* **2016**, *11*, 845; b) C. Zhu, Y. Chen, F. Liu, S. Zheng, X. Li, A. Chaturvedi, J. Zhou, Q. Fu, Y. He, Q. Zeng, *ACS Nano* **2018**, *12*, 11203.
[28] T. Patel, J. Okamoto, T. Dekker, B. Yang, J. Gao, X. Luo, W. Lu, Y. Sun, A. W. Tsen, *Nano Lett.* **2020**, *20*, 7200.
[29] H. Chen, A. Avishai, M. Surendran, J. Ravichandran, *ACS Appl. Electron. Mater.* **2022**, *4*, 5550.
[30] H. Lee, H. McKinzie, D. Tannhauser, A. Wold, *J. Appl. Phys.* **1969**, *40*, 602.
[31] G. Kresse, J. Furthmüller, *Comput. Mater. Sci.* **1996**, *6*, 15.
[32] P. E. Blöchl, *Phys. Rev. B* **1994**, *50*, 17953.
[33] J. P. Perdew, K. Burke, M. Ernzerhof, *Phys. Rev. Lett.* **1996**, *77*, 3865.
[34] H. J. Monkhorst, J. D. Pack, *Phys. Rev. B* **1976**, *13*, 5188.
[35] S. Baroni, S. De Gironcoli, A. Dal Corso, P. Giannozzi, *Rev. Mod. Phys.* **2001**, *73*, 515.


© 2023 The Authors. Advanced Materials published by Wiley-VCH GmbH

15214095, 2023, 49, Downloaded from https://onlinelibrary.wiley.com/doi/10.1002/adma.202303283, Wiley Online Library on [05/09/2024]. See the Terms and Conditions (https://onlinelibrary.wiley.com/terms-and-conditions) on Wiley Online Library for rules of use; OA articles are governed by the applicable Creative Commons License